QUANTUM MATERIALS

Quantum units from the topological engineering of molecular graphenoids

Federico Lombardi[1], Alessandro Lodi[1], Ji Ma[2], Junzhi Liu[2]*, Michael Slota[1], Akimitsu Narita[3]†, William K. Myers[4], Klaus Müllen[3]‡, Xinliang Feng[2], Lapo Bogani[1]§
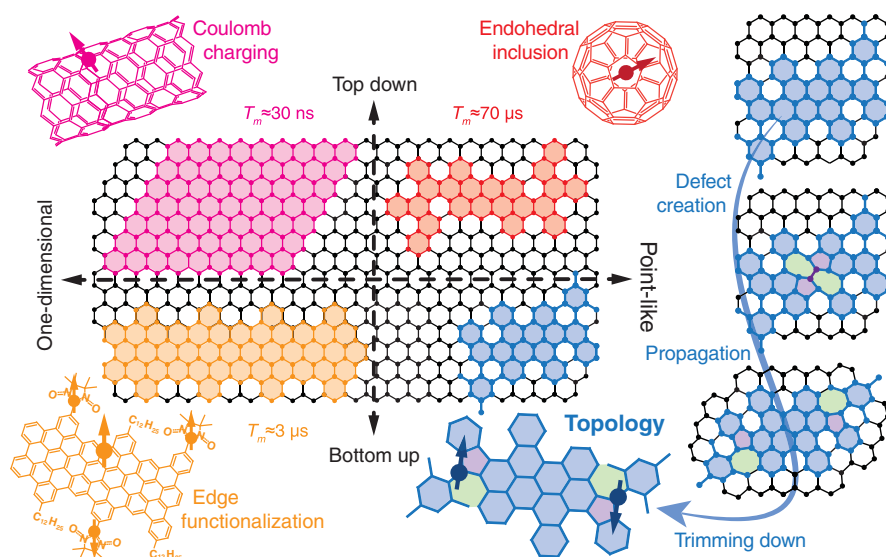
Robustly coherent spin centers that can be integrated into devices are a key ingredient of quantum technologies. Vacancies in semiconductors are excellent candidates, and theory predicts that defects in conjugated carbon materials should also display long coherence times. However, the quantum performance of carbon nanostructures has remained stunted by an inability to alter the sp^2-carbon lattice with atomic precision. Here, we demonstrate that topological tailoring leads to superior quantum performance in molecular graphene nanostructures. We unravel the decoherence mechanisms, quantify nuclear and environmental effects, and observe spin-coherence times that outclass most nanomaterials. These results validate long-standing assumptions on the coherent behavior of topological defects in graphene and open up the possibility of introducing controlled quantum-coherent centers in the upcoming generation of carbon-based optoelectronic, electronic, and bioactive systems.

Current hopes of developing radically new technologies (1, 2) in computation, communications, security, and sensing rely on the quantum manipulation of charges (3), spins (4), or photons (5). One of the main approaches is defect engineering (1, 2), which has produced robust quantum systems in diamond and silicon carbide. Conjugated sp^2-carbon nanomaterials would, in principle, be extremely appealing for quantum applications because they can be integrated into engineered devices (6) and possess intriguing mechanical (7) and transport properties (8). Methods to add spins to carbon nanomaterials include encaging heteroatoms inside fullerenes (9), confining electrons into carbon nanotubes (10), and functionalizing graphene nanoribbons (Fig. 1) (11). The manipulation of the honeycomb lattice (12, 13) using topological defects (14) is the approach that has seen most theoretical attention and could provide robustness against decoherence (15), single-photon optical control (16), and spintronic manipulation (17). On the other hand, the difficulty of reliably engineering point defects leaves it largely unexplored.

The desired level of control of the graphene lattice has become possible only recently, with the synthesis of molecules containing many fused rings in an sp^2-carbon framework (18), where pentagonal rings can be introduced reliably at precise positions (19). It is useful to relate these structures, obtained with bottom-up synthesis, to their equivalents on a graphene lattice (Fig. 1). After two (1,0) dislocations form (Stone-Wales defect), the heptagon-pentagon pairs can migrate. The lattice can then be trimmed down along the graphene stripe containing the dislocations to the desired geometry. Chemical stabilization by reso-

nance will still occur, but the resonance structure with the most disjoint benzene-like moieties is the most relevant (Clar's π-sextet rule) (16). The resulting extended open-shell molecule, with singlet and triplet states separated (20) by an energy gap 2J, is, in essence, one small graphene quantum dot with topology and defect positions shaped with atomic precision. Although the associated chemistry is seeing a veritable explosion for optoelectronic, biological, and energy applications (21), the potential of these molecules for quantum devices remains unexplored and untapped.

Our molecule of choice is a saddle-shaped diindeno-fused bischrysene (1) with highly stable open-shell biradical feature (22) (Fig. 2A). It contains a conjugated aromatic backbone and two pentagonal rings; as compared with the perfect heptagon-pentagon pairs, the difference is an unformed bond in each heptagonal ring. It is synthesized from the 11,11′-dibromo-5,5′-bichrysene (S1) in five steps (Fig. 2A and supplementary materials). The synthesis of such radicaloids has one often-overlooked feature: Incomplete dehydrogenation in the final step can lead to open-shell monoradical species (1b) at impurity concentrations, which are hard to identify by structural characterization methods. For instance, because 1b differs by one single hydrogen, it cannot be completely removed from 1 and is undetectable by mass spectrometry. For our purposes, 1b is useful because it allows for determining the behavior of single pentagonal

[1]Department of Materials, University of Oxford, 16 Parks Road, OX1 3PH Oxford, UK. [2]Center for Advancing Electronics Dresden (cfaed), Faculty of Chemistry and Food Chemistry, Technische Universität Dresden, Mommsenstraße 4, 01069 Dresden, Germany. [3]Max Planck Institut für Polymerforschung, Ackermannweg 10, 55128 Mainz, Germany. [4]Inorganic Chemistry, University of Oxford, South Parks Road, OX1 3QR Oxford, UK.
*Present address: Department of Chemistry and State Key Laboratory of Synthetic Chemistry, The University of Hong Kong, Pokfulam Road, Hong Kong, China. †Present address: Organic and Carbon Nanomaterials Unit, Okinawa Institute of Science and Technology Graduate University, 1919-1 Tancha, Onna-son, Kunigami, Okinawa 904-0495, Japan. ‡Present address: Institute of Physical Chemistry, Johannes Gutenberg-University Mainz, Duesbergweg 10-14, D-55128 Mainz, Germany.
§Corresponding author. Email: lapo.bogani@materials.ox.ac.uk

Fig. 1. Strategies toward obtaining aromatic quantum units. Quantum spin properties are introduced by heteroatom inclusion for endohedral fullerenes (red), Coulomb charging for carbon-nanotubes (magenta), and side-functionalization in graphene nanoribbons (orange). Coherence times refer to room temperature, except for carbon nanotubes (mK). Topological stabilization of magnetic centers is obtained by rational synthetic tailoring of the lattice with atomic precision at preconceived sites (blue). The result is akin to a sequence (right) of introducing a Stone-Wales defect (purple and green), followed by propagation and trimming down.

elements in the honeycomb lattice—that is, a positive disclination—which is particularly relevant at graphene edges (*23*). Although the signal from **1b** is overshadowed by **1** at room temperature, it is selectively addressable at low temperature, *T*, where **1** is completely in the singlet state.

The room-temperature electron paramagnetic resonance (EPR) spectrum shows a single peak of width 0.8 mT in a magnetic field and electron Landé factor $g = 2.0027 \pm 0.0002$ (Fig. 2B). This matches the expected signal for completely delocalized unpaired electrons in graphene, where dipolar and hyperfine couplings are weak (*24*). The linewidth (<1 mT) is incompatible with metal ions and analogous to the signals reported for radicaloids (*20–22*). Simulation with a spin $S = 1$ in the high-

exchange limit provides excellent agreement. Interestingly, no half-field signal is observed, nor any fine structure, possibly indicating a curvature-induced spin-orbit coupling higher than our accessible energy scale (*25*), as is the case for the curvature displayed by **1**. The integrated EPR signal decreases rapidly on lowering *T* and levels off at ~90 K, below which temperature **1b** is selectively addressable (Fig. 2C). Fitting with the Bleaney-Bowers equation (*11*) plus a paramagnetic species indicates that ~2% of the molecules are **1b** and that **1** has an antiferromagnetic $2J = 50 \pm 2$ meV.

The quantum evolution of a spin is often visualized as a movement over the Bloch sphere: Zenith positions indicate pure $|1/2\rangle$ and $|-1/2\rangle$ states, and any possible quantum state $|\sigma\rangle = \cos\left(\frac{\vartheta}{2}\right)|\frac{1}{2}\rangle + e^{i\varphi}\sin\left(\frac{\vartheta}{2}\right)|-\frac{1}{2}\rangle$ is represented by a
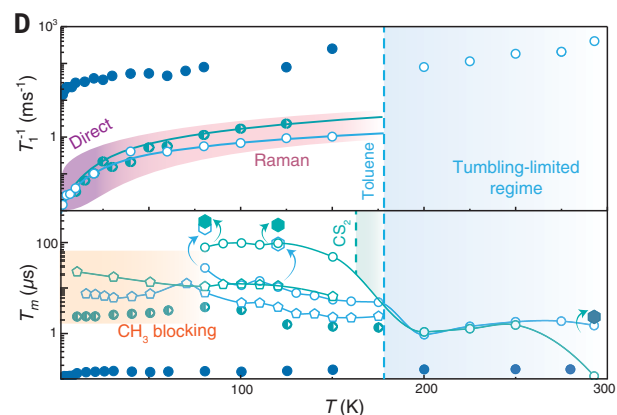
point on the spherical surface. The spin-flip time, T_1, represents vertical displacement (variations of ϑ), whereas the evolution of the quantum phase φ is described by the azimuthal movement and the associated time T_2. We measure T_1 with inversion recovery (*26*) and a lower bound of T_2 that also contains spin- and spectral-diffusion effects that are absent in single-molecule measurements, called T_m, by the Hahn-echo sequence (Fig. 3A). The coherence times of the two species, when discernible, are hereby labeled T_{m1} and T_{m1b}. We fit the spin recovery via a biexponential function (Fig. 3B and supplementary materials) and the Hahn-echo decay with the function $Y(\tau) = Y_0\left[\xi_1 e^{-\left(\frac{2\tau}{T_{m1}}\right)^x} + \xi_{1b}e^{-\left(\frac{2\tau}{T_{m1b}}\right)^x}\right]\Xi$, where $Y(\tau)$ is the echo signal, $Y_0 = Y(\tau = 0)$, and
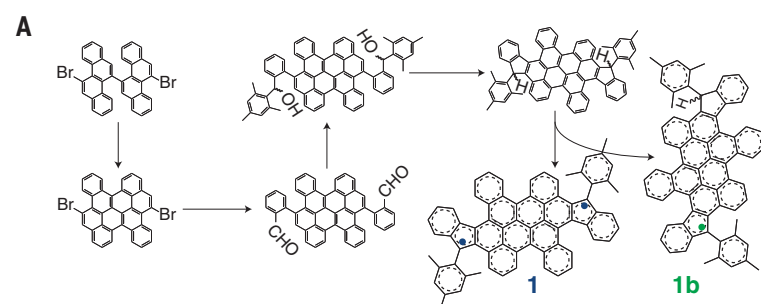
Fig. 2. Polycyclic aromatic radicaloids. (**A**) Synthesis of **1**, including the monoradical **1b**, produced by incomplete dehydrogenation in the final step. (**B**) EPR spectrum of **1** (blue) and simulation (black). *B*, static magnetic field. (**C**) Temperature-dependence of the integrated EPR intensity (circles), fitted to a Bleaney-Bowers equation (black line). The bottom panel displays the signal fraction ξ produced, at every temperature, by **1** (blue) and by **1b** (green). The error bars arise from uncertainties in the quality factor of the resonator.
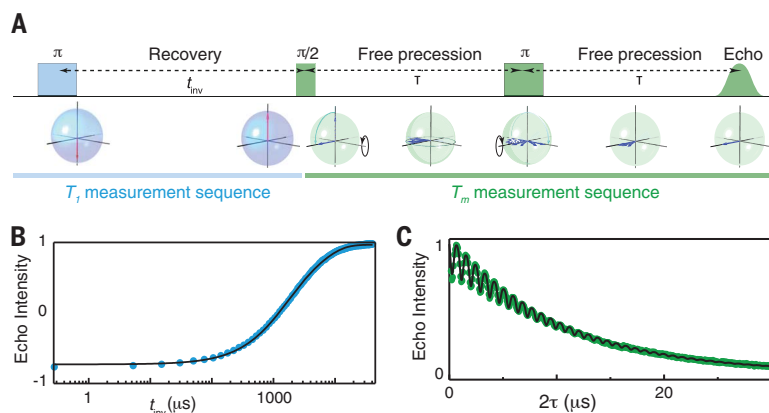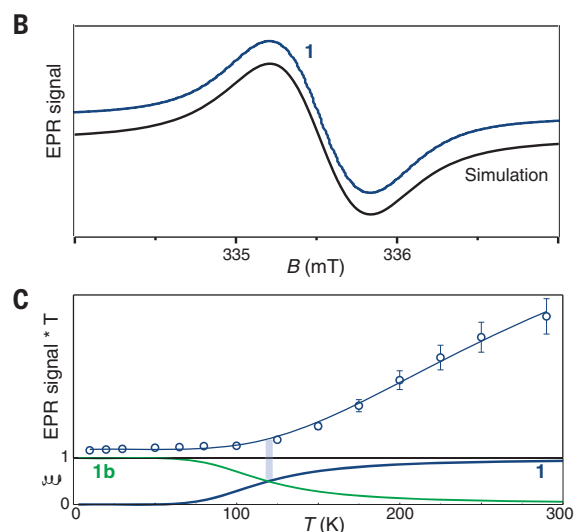

Fig. 3. Spin-lattice and coherence times. (**A**) Pulse sequence used for the detection of the spin-lattice (azure) and coherence (green) times, together with a Bloch sphere representation. t_{inv}, recovery time. (**B**) Example of signal recovery, from which T_1 is extracted (*T* = 100 K; line is fit to the data, see text). (**C**) Hahn-echo intensity versus delay time, from which T_m is extracted (*T* = 100 K; line is fit to the data, see text). (**D**) Temperature dependence of the inverse spin-lattice relaxation time (top) and of the spin coherence time

(bottom) in powders (blue full circles), toluene (green half-filled circles), *d*-toluene (blue open symbols), and CS_2 (green open symbols). Circles represent **1**, and pentagons represent **1b**. Arrows and full hexagons represent values with nuclear decoupling (Fig. 4). Errors are smaller than the symbols. Lines for T_1 are fits to the data (see text), with the different dynamic regimes shaded. Lines for T_m are guides to the eye. Vertical dashed lines indicate the freezing temperatures of toluene and CS_2.

Fig. 4. Rabi oscillations and nuclear demodulation. (**A**) Pulse sequence for the measurement of Rabi oscillations. The nutation pulse length T_p is tuned so as to vary the azimuthal position on the Bloch sphere, followed by detection. (**B**) Echo intensity versus T_p, at different pulse powers ($T = 80$ K). Black lines are fits to the data. (**C**) Spectral composition of the time-domain data showing the quadratic dependence of the Rabi frequency on the microwave power (dashed) and the power-independent ^{1}H frequency. (**D**) Pulse sequence used to progressively cancel the dephasing effect of all nuclei (orange) with Larmor precession time τ_π, leading to multiple echoes. (**E**) Echo signal decays at $T = 120$ K without (brown represents d-toluene, and orange represents CS_2) and with nuclear decoupling, with interpulse spacing $\tau_\pi = 840$ ns for d-toluene (blue) and $\tau_\pi = 680$ ns for CS_2 (green). The corresponding coherence times are reported beside the curves.
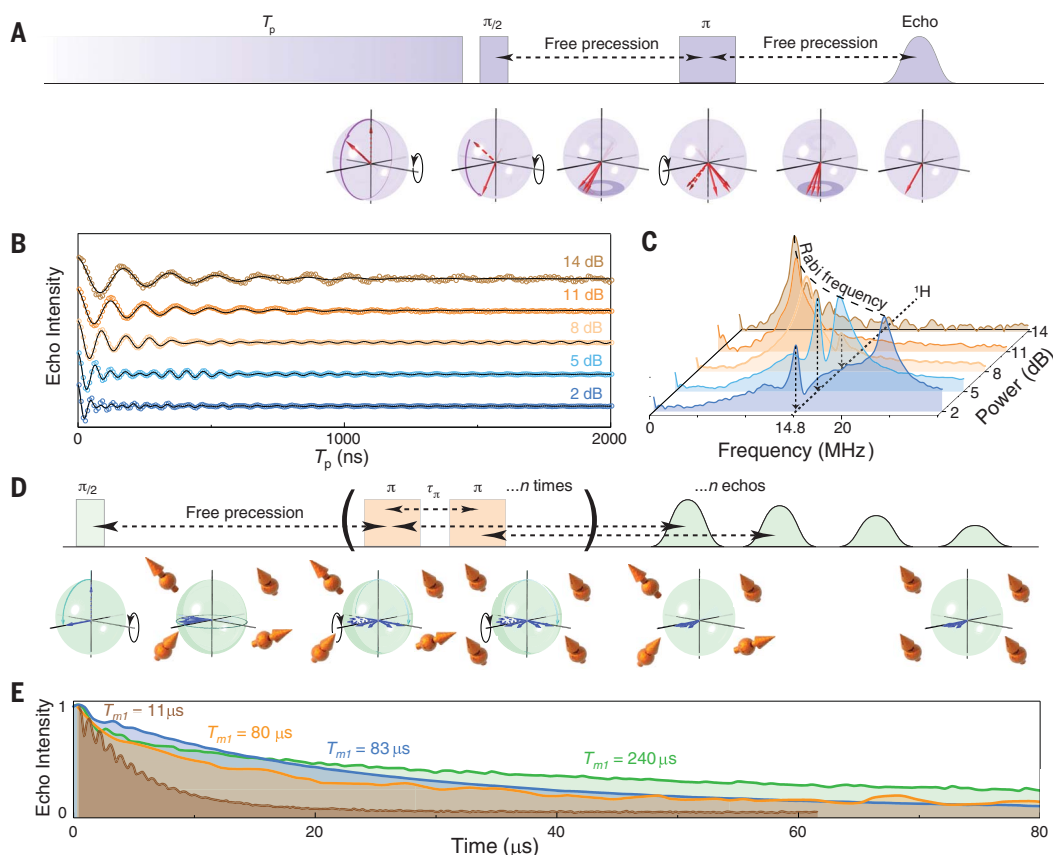
ξ_1 and $\xi_{1b} = 1 - \xi_1$ are the weights of **1** and **1b**, from Fig. 2C. $\Xi = [1 + k_1\sin(2\omega\tau + \varphi_1) + k_2\sin(4\omega\tau + \varphi_2)]$ does not affect the extracted decoherence, describing the modulation at a nucleus-specific frequency $\omega/2\pi = 14.8$ MHz for ^{1}H and 2.4 MHz for ^{2}H, with amplitudes k_1 and k_2 and phases φ_1 and φ_2 for first- and second-order effects (Fig. 3C). Good agreement is always found with stretching parameter $0.9 < x < 1$ (27).

The spin environment strongly affects both T_1 and T_2: For example, the coherence time of anionic nitrogen-vacancy-pair defects is severely suppressed when in close proximity to the diamond surface (28). Hereafter, we thus assess the behavior of **1** and **1b** in crystalline powders and toluene, deuterated-toluene, and carbon disulfide (CS_2) solutions (Fig. 3D).

For powders, T_1 increases from 1 μs at room temperature to 100 μs at 5 K, in overall agreement with semiconductors (29, 30). Both spectral diffusion and intermolecular electronic effects, such as π-stacking interactions, likely limit T_1 in such a closely packed arrangement in the solid state, and dissolution into solvents produces a 1000-fold increase in T_1, up to 1 s at 5 K. In solutions, T_1 is limited by molecular tumbling and increases only slightly on lowering T. At lower temperatures (170 K for toluene and 160 K for CS_2), the solvents turn into a glassy matrix and a two-phonon Raman pro-

cess becomes dominant down to 15 K, below which direct processes dominate the spin-flip mechanism. Good agreement (Fig. 3D) is obtained with the expression $T_1^{-1} = A_{dir}T + A_{Ram}\left(\frac{T}{\vartheta_D}\right)^9\int_0^{\vartheta_D/T}x^8e^x/(e^x-1)^2dx$, where A_i are weights for the two processes and ϑ_D is the Debye temperature (11). In the solid state, $\Xi = 1$ and $Y(\tau)$ is monoexponential, yielding $T_m \approx 300$ ns in the whole T range. Dipolar and hyperfine interactions cannot be solely responsible for the decoherence mechanism; were this true, T_m would increase and approach the CS_2 solution value below 80 K, where only **1b** contributes, and a modulation of the echo decay would be observed (e.g., as in Fig. 3C). Decoherence is likely driven by electron-electron scattering along the π-stacks, which are broken up by solvation. In this sense, these molecular systems behave differently from very-large-bandgap semiconductors—for example, diamond—and rational chemical design eliminating the π-stacking interactions could improve the solid-state coherence.

The suppression of stacking by solvation increases T_m more than 30-fold, and reduction of the solvent nuclear bath by deuteration and by CS_2 produces a further increase. Several T_m-limiting mechanisms can be identified. Above the solvent freezing point, $\Xi = 1$ and $Y(\tau)$ is monoexponential, because molecular tumbling

limits both T_m and T_1. Upon freezing, Ξ reveals hyperfine modulation by ^{1}H and ^{2}H and no modulation for CS_2, showing dominant solvent hyperfine coupling. In toluene, $Y(\tau)$ is always monoexponential, whereas in d-toluene and CS_2, the suppression of solvent ^{1}H-hyperfine interactions allows for resolving both T_{m1} and T_{m1b}, and $Y(\tau)$ is biexponential wherever **1** and **1b** coexist. T_{m1b} displays a maximum, with the low-T behavior dominated by decoherence via intramolecular hyperfine coupling and modulated by the progressive blocking of the methyl rotational motion (31). In d-toluene, T_{m1} is found to rise steadily up to 28 μs at 80 K, and in CS_2, the same trend is found but with much improved times, with T_{m1} reaching 0.1 ms at $T = 90$ K.

To verify that the spins can be initialized into an arbitrary superposition of states, we performed nutation experiments (Fig. 4A), detecting Rabi oscillation decays (Fig. 4B) (32). Fourier analysis confirms the quantum behavior, with the Rabi frequency proportional to the square root of the applied power (Fig. 4C). Because $2J \sim 10$ THz is much higher than the 10- to 100-MHz driving, which is in turn much higher than the axial spin anisotropy, no unusual evolution of the Rabi is expected (33), as is indeed observed. This analysis also indicates how to improve coherence: The power-independent peak at 14.8 MHz

3 of 4

corresponds to the ^{1}H Larmor frequency, meaning that microwave initialization pulses can also drive and decouple the nuclei—for example, by a train of π-pulses, with interpulse intervals τ_π that are multiples of the inverse of the nuclear Larmor frequency, $1/\nu_L$ (Fig. 4D) (34). In d-toluene, decoupling from the solvent nuclei yields a fivefold improvement, producing times comparable to those in CS_2 (e.g., $T_{m1b} = 38$ μs and $T_{m1} = 260$ μs at 80 K). The role of the intramolecular hyperfine interactions is revealed by decoupling from the molecular hydrogens in CS_2: We observe a threefold increase of the coherence, up to $T_{m1} = 290$ μs at 80 K. At room temperature, the decoupling allows for reaching $T_m = 2$ μs, close to the maximum attainable limit $2T_1 = 4.5$ μs.

These observations confirm experimentally the possibility of superior quantum performance in carbon-based nanostructures. The coherence times, although still below those of defects implanted deep into bulk semiconductors (1, 2, 35) and semiconducting quantum dots at millikelvin temperatures (36), outshine the latter at high temperatures and show overall agreement with predictions for graphene quantum dots with >10 nuclear spins (37). Although the quantum performance already beats the quantum behavior of diamonoids and shallowly implanted defects (25), there is ample room for optimization: The measured room-temperature values are limited by tumbling in the solvent, and very basic optimization—for example, by immobilization in an oriented diamagnetic matrix or on surfaces—is likely to produce large improvements. These results can now be used to reconsider the quantum magnetic states of graphene devices, where spins are introduced by similar defects (38). Chemical inclusion into conducting nanostructures, such as nanoribbons and graphene sheets, or fusing several molecules into double and multiple quantum dots, opens the path to using quantum effects in the next generation of optoelectronic, electric, and bioactive systems. When considering the body of work already dedicated to the integration of similar molecules into electronic devices and biologically relevant environments (18), these outcomes appear well within grasp. Optical detection and manipulation are particularly appealing—for example, via the observed single-photon emission (16)—and we may anticipate that these systems will evolve soon into synthetic analogs to optically active quantum centers in semiconductors. In this sense, it is crucial that these observations offer a rational synthetic pathway to add any desired functionality to a graphene quantum unit, opening up an unprecedented multitude of options for the optics and magnetism of quantum nanomaterials.

REFERENCES AND NOTES

1. M. Atatüre, D. Englund, N. Vamivakas, S.-Y. Lee, J. Wrachtrup, Nat. Rev. Mater. 3, 38–51 (2018).
2. D. D. Awschalom, L. C. Bassett, A. S. Dzurak, E. L. Hu, J. R. Petta, Science 339, 1174–1179 (2013).
3. L. M. K. Vandersypen et al., npj Quantum Inf. 3, 34 (2017).
4. A. Gaita-Ariño, F. Luis, S. Hill, E. Coronado, Nat. Chem. 11, 301–309 (2019).
5. D. D. Awschalom, R. Hanson, J. Wrachtrup, B. B. Zhou, Nat. Photonics 12, 516–527 (2018).
6. M. M. Shulaker et al., Nature 501, 526–530 (2013).
7. B. Lassagne, Y. Tarakanov, J. Kinaret, D. Garcia-Sanchez, A. Bachtold, Science 325, 1107–1110 (2009).
8. E. A. Laird et al., Rev. Mod. Phys. 87, 703–764 (2015).
9. M. Mehring, W. Scherer, A. Weidinger, Phys. Rev. Lett. 93, 206603 (2004).
10. T. Cubaynes et al., npj Quantum Inf. 5, 47 (2019).
11. M. Slota et al., Nature 557, 691–695 (2018).
12. P. Recher, B. Trauzettel, Nanotechnology 21, 302001 (2010).
13. O. V. Yazyev, S. G. Louie, Phys. Rev. B Condens. Matter Mater. Phys. 81, 195420 (2010).
14. J. C. Meyer et al., Nano Lett. 8, 3582–3586 (2008).
15. B. Trauzettel, D. V. Bulaev, D. Loss, G. Burkard, Nat. Phys. 3, 192–196 (2007).
16. S. Zhao et al., Nat. Commun. 9, 3470 (2018).
17. W. Han, R. K. Kawakami, M. Gmitra, J. Fabian, Nat. Nanotechnol. 9, 794–807 (2014).
18. A. Narita, X. Y. Wang, X. Feng, K. Müllen, Chem. Soc. Rev. 44, 6616–6643 (2015).
19. N. Martín, L. T. Scott, Chem. Soc. Rev. 44, 6397–6400 (2015).
20. Z. Zeng et al., Chem. Soc. Rev. 44, 6578–6596 (2015).
21. T. Y Gopalakrishna, W. Zeng, X. Lu, J. Wu, Chem. Commun. 54, 2186–2199 (2018).
22. J. Ma et al., Angew. Chem. Int. Ed. 56, 3280–3284 (2017).
23. J. Li et al., Sci. Adv. 4, eaaq0582 (2018).
24. S. Perumal, B. Minaev, H. Ågren, J. Chem. Phys. 136, 104702 (2012).
25. D. Huertas-Hernando, F. Guinea, A. Brataas, Phys. Rev. B Condens. Matter Mater. Phys. 74, 155426 (2006).
26. G. R. Eaton, S. S. Eaton, Multifrequency Electron Paramagnetic Resonance: Theory and Applications (Wiley, 2011).
27. J. R. Klauder, P. W. Anderson, Phys. Rev. 125, 912–932 (1962).
28. B. A. Myers, A. Ariyaratne, A. C. B. Jayich, Phys. Rev. Lett. 118, 197201 (2017).
29. V. A. Dediu, L. E. Hueso, I. Bergenti, C. Taliani, Nat. Mater. 8, 707–716 (2009).
30. C. Volk et al., Nat. Commun. 4, 1753 (2013).
31. A. Lund, S. Masaru, Eds., EPR of Free Radicals in Solids I: Trends in Methods and Applications (Progress in Theoretical Chemistry and Physics Series Book 24, Springer, 2012).
32. G. D. Fuchs et al., Nat. Phys. 6, 668–672 (2010).
33. R. Glenn, M. E. Limes, B. Saam, C. Boehme, M. E. Raikh, Phys. Rev. B Condens. Matter Mater. Phys. 87, 165205 (2013).
34. P. C. Maurer et al., Science 336, 1283–1286 (2012).
35. G. Balasubramanian et al., Nat. Mater. 8, 383–387 (2009).
36. M. Veldhorst et al., Nat. Nanotechnol. 9, 981–985 (2014).
37. J. Fischer, B. Trauzettel, D. Loss, Phys. Rev. B Condens. Matter Mater. Phys. 80, 155401 (2009).
38. R. R. Nair et al., Nat. Commun. 4, 2010 (2013).
39. F. Lombardi, L. Bogani, Dataset: Quantum units from the topological engineering of molecular graphenoids. Oxford University Research Archive (2019); doi: 10.5287/bodleian: j1EEx741w.

SUPPLEMENTARY MATERIALS

science.sciencemag.org/content/366/6469/1107/suppl/DC1
Materials and Methods
Supplementary Text
Figs. S1 to S10
References (40–43)